Reduced Thermomechanical Model of Transient Rotordynamics Resulting From Radial Rotor-Stator Contact

Coline Jacobs, Mathias Legrand, Fabrice Thouverez, Patricio Almeida

Proceedings of ASME Turbo Expo 2026
Turbomachinery Technical Conference and Exposition

June, 15–19, 2026, Milan, Italy

GT2026-176729

REDUCED THERMOMECHANICAL MODEL OF TRANSIENT ROTORDYNAMICS RESULTING FROM RADIAL ROTOR-STATOR CONTACT

Coline Jacobs[1,2,3] Mathias Legrand[2,4], Fabrice Thouverez[3], Patricio Almeida[1]

[1]Safran Helicopter Engines, Bordes, France
[2]McGill University, Structural Dynamics and Vibration Laboratory, Montreal, Canada
[3]Ecole Centrale Lyon, Laboratoire de Tribologie et Dynamique des Systèmes, Ecully, France
[4]Ecole Centrale de Nantes, CNRS GeM, UMR6183, Nantes, France

ABSTRACT

The present study focuses on the turbine transient dynamics when operating in a standalone mode. In a gas turbine engine, this state corresponds to the turbine stages being disconnected from the compressors. As a result, the rotordynamics of the turbine is governed by two opposing torques: one from aerodynamic forces, assumed constant, and the other from radial rubbing within a labyrinth seal on the turbine disc. The primary objective is to quantify the transient rotational speed and ensure it remains within the safety limits for motor integrity. Given the anticipated high levels of heat generation, it is also crucial to evaluate contact temperatures to identify regions vulnerable to melting wear. This paper presents an example in which the rotor is modeled using Timoshenko beam elements, while the stator is represented by 3D finite elements to capture the assembly details of the seal and housing components. To optimize computation time, reduction methods are applied to the stator's thermomechanical model, simplifying the contact treatment to a 2D problem. The rotor-stator system is then solved in the time domain using Carpenter algorithm, which predicts a response in backward precessional motion with intermittent contact before transitioning to a dry whip regime. Frequency analysis reveals that this shift is triggered by resonance in coupled rotor-stator modes. The frictional torque ultimately reaches levels sufficient to decelerate the turbine, while also causing temperature rises above the melting point.

Keywords: rotational speed, transient, reduction methods, thermomechanical, time domain, contact, precessional motion

NOMENCLATURE

b	Boundary nodes [-]
d	Rotor-stator distance [m]
f	Frequency [Hz]
h	Time step [s]
ϕ	Polar coordinate [°]
λ	Lagrange multiplier [N]
μ	Coulomb friction coefficient [-]
τ/M	Torque / Moment [N m]
T	Temperature [°C]
Ω	Rotational velocity [rad/s]
e_{rel}	Relative error [%]
g_0	Initial gap [m]
(X, Y, Z)	Fixed frame [-]
I_p	Polar second moment of area [m^4]
(J_d, J_p)	Diametral and polar mass moments of inertia [kg m^2]
(u, v, w)	Displacements in fixed frame [m]
$(\theta_u, \theta_v, \theta_w)$	Euler rotation angles
$\mathbf{v}$	Generalized velocity coordinates [m/s, rad/s]
$\mathbf{q}$	Generalized displacement coordinates [m, rad]
$\mathbf{f}$	Efforts/ torque vector [N, N m]
m / $\mathbf{M}$	Mass/ matrix [kg]
k / $\mathbf{K}$	Stiffness / Stiffness or conductivity matrix [N/m,W/°C]
c / $\mathbf{D}$	Damping / Damping or specific heat matrix [N s/kg, W s/°C]
$\mathbf{n}$, $\mathbf{t}$	Normal and tangential unit vectors in contact local frame

Superscripts and subscripts

N, T	normal and tangential components
s, t, b, l, c	stator, turbine, bearing, labyrinth, contact
D	Turbine disc (as point mass)
ext	external
fus	fusion
lim	limit

1. CONTEXT AND BACKGROUND MATERIAL

In gas generator engines, the interlocking of the turbine and compressor impellers is achieved through a tie rod (i.e., shaft), secured at both ends with nuts. The shaft may fail, disrupting the mechanical coupling between the compressor and the turbine stages. This condition, known as a shaft failure or "loss of load," [1]

is an accidental scenario where the system becomes unbalanced. The turbine continues to gain mechanical energy as it is still driven by hot gases, which can lead to uncontrolled turbine acceleration. Various studies have explored ways to limit the turbine's rotational speed in such events. Gallar [2] and Soria [1, 3], for instance, note that reducing aerodynamic efficiency, by inducing surging or adjusting the angle of incidence at the turbine blade's leading edge, can help control the speed transient.

Rotor-stator contacts, due to friction and heat generation, are other effective means of braking the turbine. Most studied contacts are axial in nature, such as disc rubbing or blade tangling [1, 3, 4]. Subsequently, other contacts may appear elsewhere in the turbine, particularly at the blade level, such as blade-casing (radial direction) and blade-vane (axial direction) contacts. In all these studies, radial contacts at the shaft level, for instance in the labyrinth seals, are neglected due to the small leverage available in comparison with the blading. However, significant contact efforts and temperatures are still expected, given the gas generator high speed. Experimental results and theoretical models in the literature indicate that a rotor confined within a stator can produce rubbing mechanisms and display a variety of complex dynamical behaviors [5–8]. Generally, the rotor's motion is described by (1) lateral vibrations of the structure (defined by the precessional speed) and (2) rotation with an angular velocity Ω [6]. When the structure moves in the same direction as Ω, it is known as forward precessional motion, where the circumferential or precessional velocity aligns with Ω. Conversely, when the precessional velocity opposes Ω, is characteristic of backward precessional motion. In instances of fully annular rub, backward motion is further divided into two subcategories:

- Dry whip occurs when the rotor both rolls and slips, meaning the relative tangential velocity $\mathbf{v}_T$ (i.e sliding speed) is non-zero. This type of response is generally undesirable in rotordynamics due to its instability and the high contact forces that may damage the contacting structures [6, 9, 10].
- Dry whirl takes place when the rotor rolls without sliding, implying the kinematic constraint $||\mathbf{v}_T|| = 0$.

In practice, fully annular rub does not always occur. A third type of response, partial contact, is characterized by a non-circular trajectory of the rotor and can occur in both forward and backward precessional motions [11, 12]. Based on a previous model developed by the authors [13], it is anticipated that transition types involving contact separation will occur. The present paper proposes a novel combination of transient rotordynamics for a standalone turbine configuration, radial rubbing contact at the shaft level, thermomechanical and bending-torsion couplings, and 3D model reduction. These last two aspects are improvements from the authors previous works [13, 14].

A standalone turbine is a simplified theoretical case where the turbine operates autonomously. It is no longer connected to the compressor, implying that the turbine shaft is only supported by the rear bearing and the rotor-stator contact. In the remainder of the document, it is assumed that only one labyrinth tooth makes contact, although in practice, a labyrinth seal consists of several teeth. For simplicity of vocabulary, the term labyrinth refers to the annular tooth, while its envelope is defined as the ring.

2. STATOR MODEL

2.1 Geometry and assumptions

The stator consists of several parts to reflect an industrial assembly as depicted in Figure 1. It includes the T-section ring that serves as the envelope of the labyrinth (ring) as well as the diffuser and the distributor of the high pressure stage, to which the ring is attached. Two bonded contact areas are defined at the interfaces between the parts. In practice, the three parts assembly is made by screws, which have been neglected in the model. Concerning the boundary conditions, the stator does not undergo

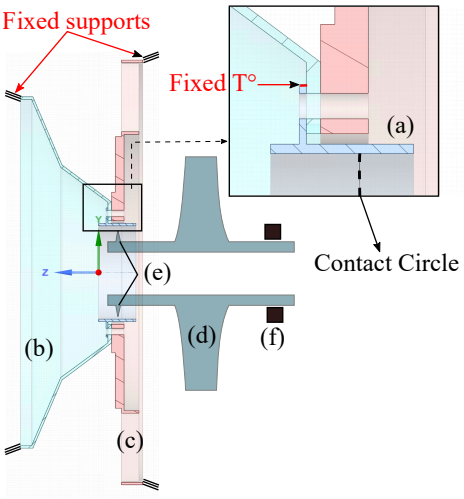

FIGURE 1: Rotor-stator system with boundary conditions and contact zone: (a) ring, (b) diffuser, (c) distributor, (d) turbine, (e) labyrinth, (f) rear bearing.

any preload. Rigid body movements are eliminated by fixing the outer faces of the diffuser and the distributor (see Figure 1). Finite elements approach is used to discretize the stator in space. The diffuser and the distributor contribute only to the mechanics of the problem. Once meshed, the nodes of these parts have three degrees of freedom (dofs) in translation (u, v, w). the ring nodes get an additional thermal degree of freedom T. Given the fast dynamics of the contact ($t < 0.5\,\mathrm{s}$), it is acceptable to assume fixed temperature far from the contact interface. Therefore, the temperature is fixed at the end of the ring branch described in Figure 1. The stator material is standard steel provided in ANSYS technical data (*Structural steel*) and is assigned to the three components. Defining $\mathbf{q}_s$ and $\mathbf{T}$ as the mechanical and thermal dofs, the thermomechanical finite element model of the stator reads

$$\begin{pmatrix} \mathbf{M}_s^{qq} & 0 \\ 0 & 0 \end{pmatrix} \begin{pmatrix} \ddot{\mathbf{q}}_s \\ \dot{\mathbf{T}} \end{pmatrix} + \begin{pmatrix} \mathbf{D}_s^{qq} & 0 \\ 0 & \mathbf{D}^{\vartheta\vartheta} \end{pmatrix} \begin{pmatrix} \dot{\mathbf{q}}_s \\ \dot{\mathbf{T}} \end{pmatrix} + \begin{pmatrix} \mathbf{K}_s^{qq} & \mathbf{K}^{q\vartheta} \\ 0 & \mathbf{K}^{\vartheta\vartheta} \end{pmatrix} \begin{pmatrix} \mathbf{q}_s \\ \mathbf{T} \end{pmatrix} = \begin{pmatrix} \mathbf{f}_c \\ \dot{\mathbf{Q}}_c \end{pmatrix} \quad (1)$$

where $\mathbf{M}^{qq}$, $\mathbf{D}^{qq}$ and $\mathbf{K}^{qq}$ are the mass, damping, and stiffness matrices, $\mathbf{D}^{\vartheta\vartheta}$ and $\mathbf{K}^{\vartheta\vartheta}$ are the specific heat and thermal conductivity matrices. The coupling between physics is represented by the thermal expansion matrix $\mathbf{K}^{q\vartheta}$ and heat rates vector $\dot{\mathbf{Q}}_c$ generated by contact forces $\mathbf{f}_c$. The latter includes the normal force $\mathbf{f}_N$ and friction force $\mathbf{f}_T$ (where the index T indicates that friction acts in the tangential direction). As in many works [15–18], friction is modeled here by Coulomb's law only in the sliding

phase and opposite to the tangential relative velocity $\mathbf{v}_\mathrm{T}$, giving $\mathbf{f}_\mathrm{T} = -\mu||\mathbf{f}_\mathrm{N}||\frac{\mathbf{v}_\mathrm{T}}{||\mathbf{v}_\mathrm{T}||}$. In this article, the thermal study is conducted only on the stator. When conductance and wear effects are ignored, as considered in this paper, it is common to assume that heat is generated only by friction and is equally partitioned between the rotor and stator [15, 19, 20]. In this case, the heat rate vector is computed as the following element-wise product[1]

$$\dot{\mathbf{Q}}_c = -0.5\mu\mathbf{v}_\mathrm{T} \circ \mathbf{f}_\mathrm{T}. \tag{2}$$

All the vectors above are functions of time in practice but this dependence is dropped to simplify notations. As a result, the total energy generated by friction, noted W_f is assessed though

$$W_f = 2\int_0^t \mathbf{1}^\top \dot{\mathbf{Q}}_c \mathrm{d}t = -\mu \int_0^t \mathbf{v}_\mathrm{T}^\top \mathbf{f}_\mathrm{T} \mathrm{d}t, \tag{3}$$

where $\mathbf{1}$ is a column vector filled with ones.

2.2 Thermomechanical reduction of the stator

After applying the boundary conditions, the thermomechanical model has 75120 mechanical dofs and 3390 thermal dofs. In the scope of further time discretization, a system of this size requires a very low time step, leading to prohibitive computation times in an industrial context[2]. Thus, it is decided to implement a thermomechanical superelement for the stator. Typically, the nodal quantities (displacements, temperatures) of a finite element model are divided into two categories. The first one gathers the nodes designated as boundary (or master) nodes. These are the nodes retained in the reduced basis because they are useful for application of boundary conditions (contact interface in the present work). The rest of the nodes are considered internal. Their contribution to the dynamics/thermal behavior of the substructure is approximated based on responses to specific boundary conditions and loads. As already mentionned in the introduction, a single labyrinth tooth is considered on the turbine shaft (cf Figure 1). When ignoring axial displacement and rotation of the tooth, the contact interface is limited to a circle on the ring inner radius. The labyrinth and the contact circle have the same axial position on the shaft line. This circle thus defines the position of the master nodes for model reduction. A preliminary step to any reduction is to rearrange the vector of nodal quantities and the matrices of Equation (1) between master nodes (subscript b for boundary) and internal nodes (subscript i). The most commonly used method in structural dynamics is Craig-Bampton [21]. The associated reduction matrix is written as:

$$\mathbf{R}_\mathrm{CB} = \begin{pmatrix} \mathbf{I}_{bb} & \mathbf{0}_{b\eta} \\ \mathbf{K}_{ii}^{-1}\mathbf{K}_{ib} & \Phi_{i\eta} \end{pmatrix} \tag{4}$$

with $\mathbf{K}$ the stiffness matrix and $\Phi_{i\eta}$ the truncated basis of the first η fixed interface modes. However, not all reduction methods are suitable for all physical phenomena. This can be partly explained by the different nature of the equations, hyperbolic for vibration and parabolic for heat. It has been shown that this approach presents poor results for the heat equation, especially for high-frequency excitation, as in the case of frictional contact [22]. Indeed, achieving convergence with the reduced model requires retaining a large number of modes, which makes the reduction inefficient. Recent work [23] proposed a reduction method for a thermomechanical issue using Craig-Bampton for the mechanical part and static condensation for the thermal part. However, the aim of this research was to calculate the steady-state response in the frequency domain. Heat was considered stationary, and the specific heat matrix was neglected, which is not suitable for the objectives of this work. The chosen reduction approach was developed by Guérin [24] who proceeded with a decoupled substructuring. Decoupling means that the mechanical modes do not account for dilatation and that the reduction submatrices can be created for each physics separately with the most suitable method. Craig-Bampton method is selected for mechanics and Rational Craig-Hale (RCH) for heat. The Craig and Hale [25] approach combines modal reduction and block Krylov methods [26] for a system whose interface is considered fixed. Without going into detail, the Craig-Hale method consists of approximating the transfer function ($H(s) = F(C(t), K(t))$) of a system by a Taylor series expansion to order l around the Fourier variable $s = 0$. The matrix terms then form a basis named $\mathbf{P}$ of size $i \times b(l+1)$. For more information about the method to form the basis, please refer to [24] . This basis, to be well-conditioned and keep a reasonable size, undergoes a Singular Value Decomposition (SVD) [27] to eliminate linearly dependent columns. The resulting matrix is noted as such and allows constructing the final reduction matrix and its associated reduction matrix as:

$$\mathbf{R}_\mathrm{CH} = \begin{pmatrix} I_{bb} & 0 \\ \mathbf{K}_{ib}\mathbf{K}_{ii}^{-1} & \mathrm{SVD}(\mathbf{P}) \end{pmatrix} \tag{5}$$

where we see again the static modes base. The particularity of the RCH method is that this development is calculated at multiple s values. For p points of expansion, basis $\mathbf{P}$ before SVD is thus made of $b(l+1)p$ columns. The interest of this augmentation is a better characterization of high-frequency thermal behavior, which is expected in the context of rotor-stator contact. Indeed, in this case, the heat source frequency is linked to the structure's vibration frequency, which can be very high. The present work considers that the p expansion points have a logarithmic distribution in the frequency range $[1, 10^5]$ Hz. While this distribution type can be debated in mechanics due to natural frequencies, it seems relevant for thermal analysis. Thermal transfer function shapes are low-pass filter-like, much smoother than those obtained in dynamics, presenting many resonance and anti-resonance peaks. In this article, the mechanical reduction by Craig-Bampton is done using ANSYS's substructuring tool. The thermal reduction is not yet available, but it is possible to extract the necessary specific heat and thermal conductivity matrices to set up the RCH reduction basis. The master nodes are selected on the circle inside the stator, which has the same axial position as the labyrinth tooth mounted on the turbine. In order to obtain the best compromise between accuracy and computation time, the number of master nodes b retained in the model can be modified, and two levels of reduction are defined where $b = 36$ and $b = 72$.

Once the number of master nodes b is fixed, the number

[1] The operator $\circ$ stands for element-wise product.

[2] The conducted simulations, lasting 120 ms, required up to 5 days of runtime with reduced models. Without this reduction process, CPU time would be even longer.

of fixed-interface modes η to be retained in the Craig-Bampton reduction basis must be defined. The objective is to correctly reproduce the first 18 modes, which gives a frequency range of interest from 0 to 3500 Hz. Above this limit, modeshapes are related to the bending of distributor blades which are not relevant in the scope of rotor-stator contact. The Frequency Response Function (FRF) is investigated in Figure 2 to validate the quality of the reduction outside resonances. The colocalized FRF is calculated on a master node with excitation on the horizontal displacement. For both levels of reduction, retaining $\eta = 60$ does not alter the quality of the reduction. Indeed, the FRFs are indistinguishable from the full model[3]. The relative errors e_{rel} are almost identical and remain bounded at 3.2%, see Figure 2. This relative error is calculated as the absolute value of $\frac{\text{FRF}}{\text{FRF}_{\text{full}}} - 1$.

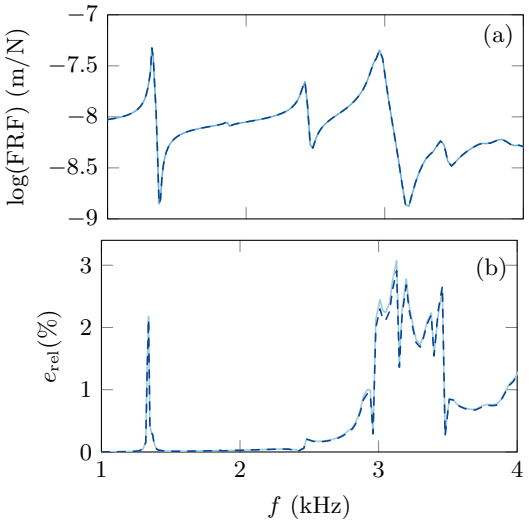

FIGURE 2: Craig-Bampton reduction with master nodes refinement $b = 36$ (——) and 72 (– –). (a) Structural FRF, (b) Relative error on FRF.

Eventually, RCH method requires to chose a proper amount of expansion points p, the expansion order l and the SVD tolerance. Their values from the parametric study are summarized in Table 1. In contrast to dynamics, the sensitivity of FRF to the number of master nodes b is more pronounced for the thermal part. Given identical reduction parameters, Figure 3 shows that the model with $b = 36$ is slightly less accurate, with relative error of 4.1%. For $b = 72$, it is found that $e_{\text{rel}} < 1.67\%$. The coarser superelement is thus expected to provide overestimated temperatures for the same amount of heat.

Parameters	Symbol	Value
Expansion points	p	6
Expansion order	l	0
Tolerance SVD	ϵ	10^{-4}

TABLE 1: Parameters of RCH reduction on heat equation

[3]To avoid costly FRF calculations, a full system is approximated by a reduced system with high amount of modes, here $\eta = 200$.

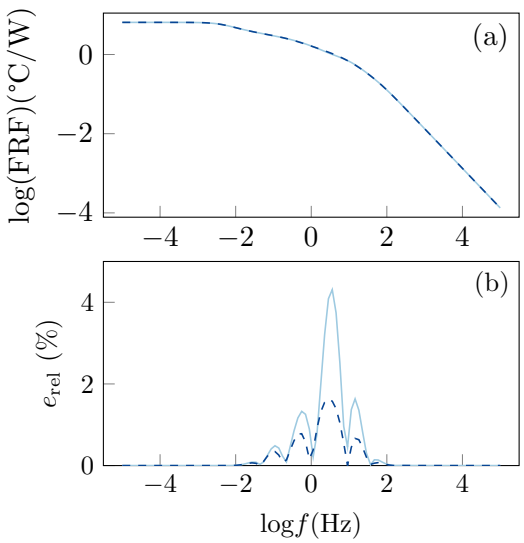

FIGURE 3: Comparison of RCH reduction with master nodes refinement $b = 36$ (——) and $b = 72$ (– –): (a) thermal FRF; (b) relative error on FRF

3. SIMPLIFIED TURBINE MODEL

The proposed turbine shaft in Figure 4 has a constant circular hollowed section in Inconel, and the disk is simplified by a point mass. The absolute reference frame (X, Y, Z) of the turbine is defined with origin on the rear bearing. The lateral rotations $\theta_u(z,t)$ and $\theta_v(z,t)$ and the rotation $\theta_w(z,t)$ follow the Euler angles formalism [17]. In the following, when not required, dependency of rotations and displacements with axial position z and time t are dropped in notations. With u, v and w being the translational dofs, and knowing the cross-sectional moments of inertia I_d and I_p, the integral expression of the kinetic energy for a constant section beam element is written as

$$2E_c = \rho \int_0^L \left[S(\dot{u}^2 + \dot{v}^2 + \dot{w}^2) + I_d(\dot{\theta}_u^2 + \dot{\theta}_v^2) + I_p \dot{\theta}_w^2 + 2I_p \dot{\theta}_w \dot{\theta}_u \theta_v \right] \mathrm{d}z. \tag{6}$$

The straight beam element model is based on Timoshenko's theory, i.e., accounting for shear deformation. For a constant beam section S, with shear modulus $G = \frac{E}{2(1+\nu)}$ determined with Young's modulus E and Poisson's ratio ν, the strain energy is given by

$$2E_d = \int_0^l \left[ES\left(\frac{\partial w}{\partial z}\right)^2 + EI_d\left(\left(\frac{\partial \theta_u}{\partial z}\right)^2 + \left(\frac{\partial \theta_v}{\partial z}\right)^2\right) + GI_p \frac{\partial^2 \beta}{\partial z^2} + k_{xy} GS\left(\left(\frac{\partial u}{\partial z} - \theta_v\right)^2 + \left(\frac{\partial v}{\partial z} + \theta_u\right)^2\right)\right] \mathrm{d}z \tag{7}$$

where k_{xy} is the shear coefficient. The angle β corresponds to the twist angle. The torsion motion is preserved since the aerodynamic torque τ_a and friction τ_f are not applied at the same place on the shaft (respectively on the disk and the labyrinth). Moreover, previous works performed by the authors showed that τ_f can largely exceed τ_a [13]. For each point along the shaft, a single rotation angle $\theta_w(z,t)$ is considered as the sum of the rigid body rotation $\varphi(t)$ common to the entire shaft and the torsion $\beta(z,t)$. By denoting $\dot{\varphi} = \Omega$, this relation translates at velocity level as $\dot{\theta}_w(z,t) = \Omega(t) + \dot{\beta}(z,t)$.

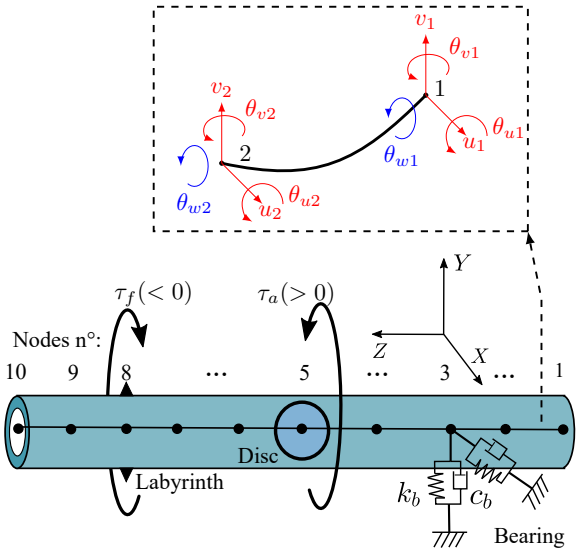

FIGURE 4: Simplified turbine model with location of driving and friction (negative) torques (τ_a, -τ_f) applied on the disc and labyrinth nodes respectively, and space discretization with beam elements

3.1 Finite elements model

A beam element where torsion is taken into account is presented in Figure 4, and has 10 dofs per element. The vector of generalized coordinates takes the form

$$\mathbf{q}^e = (u_1, v_1, \theta_{u1}, \theta_{v1}, \theta_{w1}, u_2, v_2, \theta_{u2}, \theta_{v2}, \theta_{w2})^\top. \tag{8}$$

The dofs can be organized into three vectors: displacements and rotations in the (X,Z) plane $\mathbf{q}_x^\top = (u_1, \theta_{v1}, u_2, \theta_{v2})$; degrees of freedom in the (Y,Z) plane $\mathbf{q}_y^\top = (v_1, \theta_{u1}, v_2, \theta_{u2})$, and proper rotations $\mathbf{q}_z^\top = (\theta_{w1}, \theta_{w2})$. The derivation of exact mass and inertia matrices is identical to the documentation of `code_Aster` [28, 29]. The shape functions used for bending are the same for mass and stiffness and involve the shear coefficient. Polar rotation, on the other hand, is linearly interpolated. The matrix form of the kinetic energy related to translations and rotations is given by

$$2E_{c,rt} = \mathbf{q}_x^\top (\mathbf{M}_u^e + \mathbf{M}_{\theta v}^e)\mathbf{q}_x + \mathbf{q}_y^\top (\mathbf{M}_v^e + \mathbf{M}_{\theta u}^e)\mathbf{q}_y + \mathbf{q}_z^\top \mathbf{M}_{\theta w}^e \mathbf{q}_z. \tag{9}$$

The expression of these elementary matrices is provided in Appendix A. Once the five matrices are augmented for the full element vector $\mathbf{q}^e$, their sum is condensed into the elementary matrix $\mathbf{M}_{\text{sh}}^e$.

The rotations are all approximated with shape functions: $\theta_w(z,t) \approx \mathbf{N}_z(z)\mathbf{q}_z(t)$, $\theta_u(z,t) \approx \mathbf{N}_{\theta u}(z)\mathbf{q}_y(t)$ and $\theta_v(z,t) \approx \mathbf{N}_{\theta v}(z)\mathbf{q}_x(t)$. Therefore, the difficulty of accounting for bending-torsion coupling lies in the integration of the gyroscopic term, along the element length $lene$

$$E_{c,\text{gyr}} = \rho I_p \int_0^{\ell_e} \mathbf{N}_z(z)\dot{\mathbf{q}}_z \dot{\mathbf{q}}_y^\top \mathbf{N}_{\theta u}^\top(z)\mathbf{N}_{\theta v}(z)\mathbf{q}_x \mathrm{d}z. \tag{10}$$

The computation of this term is not trivial and requires integration by parts [30] but is not developed in this article. By adding the beam stiffness matrices $\mathbf{K}_{\text{sh}}^e$ [28] and Rayleigh damping[4] $\mathbf{D}_{\text{sh}}^e = 10^{-6}\mathbf{K}_{\text{sh}}^e$, the rotordynamics is governed by

$$\begin{aligned}\mathbf{M}_{\text{sh}}^e\ddot{\mathbf{q}}^e + (\dot\theta_{w2}\mathbf{G}_1^e - (\dot\theta_{w2}-\dot\theta_{w1})\mathbf{G}_2^e + \mathbf{D}_{\text{sh}}^e)\dot{\mathbf{q}}^e \\ + (\ddot\theta_{w2}\mathbf{A}_1^e - (\ddot\theta_{w2}-\ddot\theta_{w1})\mathbf{A}_2^e + \mathbf{K}_{\text{sh}}^e)\mathbf{q}^e + \mathbf{f}_{\text{cp}}^e(\mathbf{q}^e,\dot{\mathbf{q}}^e,\ddot{\mathbf{q}}^e) = \mathbf{f}_{\text{ext}}^e.\end{aligned} \tag{11}$$

Matrices $\mathbf{A}_1^e$ and $\mathbf{A}_2^e$ do not possess any symmetry property and are given in Appendix A. The first one corresponds to the usual angular acceleration (i.e. Coriolis) matrix for a beam without torsion [29]. The classical gyroscopic matrix is defined by $\mathbf{G}_1^e = \mathbf{A}_1^e - \mathbf{A}_1^{e\top}$ and the torsion contribution is determined by the matrix $\mathbf{G}_2^e = \mathbf{A}_2^e - \mathbf{A}_2^{e\top}$. Both are antisymmetric matrices. The last coupling term is denoted as a coupling vector $\mathbf{f}_{\text{cp}}^e(\mathbf{q}^e,\dot{\mathbf{q}}^e,\ddot{\mathbf{q}}^e)$ which is nonzero only for dofs θ_{w1} and θ_{w2} (i.e. on the 5th and 10th rows, cf Equation (8)). To simplify the notation, the dependencies of the coupling term on the generalized coordinate vector $\mathbf{q}^e$ and its derivatives are not kept. After assembling all elements, the turbine's dofs are grouped into $\mathbf{q}_t$, so $\mathbf{q}_t = \cup_e \mathbf{q}^e$. Figure 4 shows that the rigid disk (point mass) is mounted on the 5th node of the shaftline. The expressions of the mass, gyroscopic and Coriolis matrices of the rigid disk (resp. $\mathbf{M}_D$, $\mathbf{G}_D$ and $\mathbf{A}_D$), as well as the coupling vector $\mathbf{f}_{\text{cp},D}$, are given in Appendix B. They are added to the corresponding dof components in Equation (11). Finally, the bearing is accounted for by adding damping c_b and stiffness k_b on the translations of the 9th node. The mass, damping, stiffness gyroscopic and Coriolis matrices for the turbine are respectively denoted $\mathbf{M}_t$, $\mathbf{D}_t$, $\mathbf{K}_t$, $\mathbf{G}_t(\ddot{\mathbf{q}}_t)$, and $\mathbf{A}_t(\ddot{\mathbf{q}}_t)$. Note that these two last matrices are not constant because of the torsion dofs. The equations of motion for the complete turbine in condensed form are

$$\mathbf{M}_t\ddot{\mathbf{q}}_t + (\mathbf{G}_t(\dot{\mathbf{q}}_t) + \mathbf{D}_t)\dot{\mathbf{q}}_t + (\mathbf{A}_t(\ddot{\mathbf{q}}_t) + \mathbf{K}_t)\mathbf{q}_t + \mathbf{f}_{\text{cp,t}} = \mathbf{f}_{\text{ext,t}} \tag{12}$$

where $\mathbf{f}_{\text{ext,t}}$ is a vector of external forces. Gravity is neglected, so this vector is zero except on the row corresponding to the rotation θ_w of the disk node. This dof undergoes a loading related to the aerodynamic torque τ_a.

4. UNILATERAL CONTACT WITH FRICTION AND HEAT

At this stage, the numerical model includes a reduced stator representative of the real assembly in the engine, and a flexible shaft line accouting for flexion-torsion coupling. The present section describes the rotor-stator interaction through unilateral frictional contact and heat generation. In what follows, the dofs of the complete system are separated into mechanical ones $\mathbf{q} = (\mathbf{q}_s, \mathbf{q}_t)^\top$ and thermal ones $\mathbf{T}$. Unilateral contact conditions prevent mechanical bodies to penetrate each other and always create a reaction force of magnitude F_{N}^j in direction $\mathbf{n}$ normal to the contact surface at master node $j = 1, \ldots, b$, as detailed in Figure 5. The distance separating the bodies evaluated at node j reads

$$d_{\text{N}}^j(\mathbf{q}) = \sqrt{(x_{s0}^j + u_{s,j} - u_l)^2 + (y_{s0}^j + v_s^j - v_l)^2} - R_l \tag{13}$$

where (x_{s0}^j, y_{s0}^j) and (u_s^j, v_s^j) are respectively the master node initial position and displacement (their sum gives (x_s^j, y_s^j)), (u_l, v_l) is the displacement of the labyrinth node and R_l the labyrinth radius. We recall that the last two pairs are indeed components of $\mathbf{q}$. A classical formulation of unilateral contact constraints is

[4] The Rayleigh coefficient 10^{-6} is a lump sum value fixed by the industrial partner.

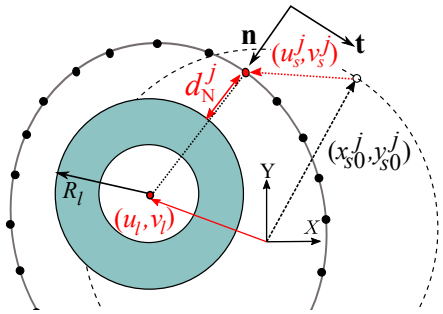

FIGURE 5: Nodal gap definition and position decomposition for a stator node j between initial (– –) and deformed (–●–) states

given by the Signorini conditions expressed at the displacement level [31]. They involve the non-penetration constraint $d_N^j \geq 0$, the non-traction constraint $F_N^j \geq 0$ and $d_N^j F_N^j = 0$, enforcing that both constraints cannot be active simultaneously. The strict enforcement of the Signorini conditions is possible via Lagrange multipliers $\boldsymbol{\lambda}$.

The complete rotor-stator system is governed by a differential equation similar to Equation (1):

$$\begin{pmatrix} \mathbf{M}^{qq} & \mathbf{0} \\ \mathbf{0} & \mathbf{0} \end{pmatrix} \begin{pmatrix} \ddot{\mathbf{q}} \\ \ddot{\mathbf{T}} \end{pmatrix} + \begin{pmatrix} \mathbf{C}^{qq} & \mathbf{0} \\ \mathbf{0} & \mathbf{C}^{\vartheta\vartheta} \end{pmatrix} \begin{pmatrix} \dot{\mathbf{q}} \\ \dot{\mathbf{T}} \end{pmatrix} + \begin{pmatrix} \mathbf{K}^{qq} & \mathbf{K}^{q\vartheta} \\ 0 & \mathbf{K}^{\vartheta\vartheta} \end{pmatrix} \begin{pmatrix} \mathbf{q} \\ \mathbf{T} \end{pmatrix} + \begin{pmatrix} \mathbf{f}_{\text{cp}} \\ 0 \end{pmatrix} = \begin{pmatrix} \mathbf{C}_{\text{NT}} \\ \mathbf{C}_{\vartheta} \end{pmatrix} \boldsymbol{\lambda}, \tag{14}$$

where $\mathbf{C}^{qq} \equiv \mathbf{C}^{qq}(\dot{\mathbf{q}})$ and $\mathbf{K}^{qq} \equiv \mathbf{K}^{qq}(\ddot{\mathbf{q}})$. Nevertheless, several differences with Equation (1) are noticed:

- the presence of nonlinearities due to the inertial and gyroscopic effects of the rotor;
- the introduction of the contribution matrices of the Lagrange multiplier vector $\boldsymbol{\lambda}$ to the mechanics and thermal, respectively noted as $\mathbf{C}_{\text{NT}}$ and $\mathbf{C}_{\vartheta}$. Their expressions are developed further in this section.

In this article, the chosen resolution method in time domain, including contact management with Lagrange multipliers, is the Carpenter algorithm [32]. The method follows a prediction-correction approach. It is widely used in the literature [11, 17, 33], and validated by test data [34]. It should be noted that each component λ^j, corresponds to the normal force at node j when solution is converged. Finally, for the specific case of a nonlinear system, which is the case here, adaptations are available [13, 17] and require an iteration of the prediction and/or correction steps in a Newton loop. Note that other approaches were tested such as Moreau-Jean [35, 36]. Corresponding results are not described as they are very similar to Carpenter.

For both Carpenter and Moreau-Jean methods, the formulation for matrices $\mathbf{C}_{\text{NT}}$ and $\mathbf{C}_{\vartheta}$ is the same and is described in the following. Each master node j is associated with a local frame $(\mathbf{n}, \mathbf{t})$, see Figure 5. The components of these unit vectors in the absolute frame (X,Y), i.e. where the thermomechanical problem is defined, are written $\mathbf{C}_{\text{N}}^j$ et $\mathbf{C}_{\text{T}}^j$. It turns out that the first vector $\mathbf{C}_{\text{N}}^j = \nabla_{\mathbf{q}} d_{\text{N}}^j(\mathbf{q})$ corresponds to the gradient of the normal distance to node j, which is already developed in Equation (13). Strictly speaking, $\mathbf{C}_{\text{N}}^j$ depends on the generalized coordinates $\mathbf{q}$ but the latter has been eliminated from the notation for conciseness. Similarly, the vector $\mathbf{C}_{\text{T}}^j$ can be defined, which contains the contributions of tangential forces, i.e., frictional forces, to the equations of motion and is orthogonal to $\mathbf{C}_{\text{N}}^j$. Vector $\mathbf{C}_{\text{T}}^j$ is also derived from a gradient of a tangential distance $\mathbf{C}_{\text{T}}^j = \nabla_{\mathbf{q}} d_{\text{T}}^j$ with

$$d_{\text{T}}^j(\mathbf{q}) = r^j \arctan \frac{v_s^j - v_l}{u_s^j - u_l} - R_l \theta_{wl}, \quad j = 1, \ldots, b \tag{15}$$

where $r^j = d_{\text{N}}^j + R_l$ is kept constant during the gradient computation. The vector $\mathbf{C}_{\text{T}}^j$ is also involved in the assessment of the tangential velocity at contact by scalar product $\text{v}_{\text{T}}^j = \mathbf{C}_{\text{T}}^{\top} \dot{\mathbf{q}}$. As a result, $\mathbf{C}_{\text{NT}} = \cup_j \mathbf{C}_{\text{N}}^j - \mu \, \text{sign}(\text{v}_{\text{T}}^j) \mathbf{C}_{\text{T}}^j$ is constructed by concatenation and embeds the Coulomb's law in sliding phase only. Matrix $\mathbf{C}_{\vartheta}$ is identified in a similar way. Based on Equation (2), heat rate entering the stator at node j reads $\dot{Q}^j = 0.5\mu |v_{\text{T}}^j| \lambda^j$. Therefore, each row of vector $\mathbf{C}_{\vartheta}^j$ is zero except for the j^{th} one equal to $0.5\mu |v_T^j|$.

5. RESULTS FOR TURBINE WITH CONSTANT SECTION

In what follows, unless otherwise noted, the contact resolution method used is that of Carpenter. As mentioned in section 2, two levels of stator reduction are studied: with 36 and 72 master nodes (b). These nodes are identified by their polar coordinate ϕ (=0°on positive X axis). For now, thermal expansion is not taken into account. Finally, the time step h for each model is chosen to ensure calculation stability: $h = 6 \times 10^{-7}$ s with 36 nodes and $h = 2 \times 10^{-7}$ s for 72 nodes.

5.1 Mechanical solution

First, it turns out that the rotational speed profiles of the disk (see Figure 6) are identical when changing the number of master nodes b. The rotational speed remains lower than $0.85\Omega_{\text{lim}}$. In the context of shaft failure, the variable Ω_{lim} is defined to guarantee the turbine disk mechanical limits. The same goes for the lateral vibration of the shaft at the labyrinth u_l illustrated in Figure 7. The curves overlap perfectly until 55 ms, which corresponds to the onset of dry whip. Beyond that, a slight phase shift exists between the responses of the two models, but the vibration levels in dry whip and dry whirl remain equal. Finally, the transient on the friction torque τ_f (cf. Figure 7) is perfectly superimposed for the partial contact phase, which is characterized by an intermittent torque. These results confirm that the reduced casing model with

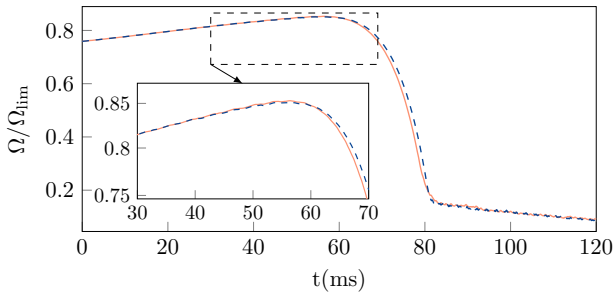

FIGURE 6: Rotational speed response of the disc with 36 (——) and 72 (– –) a master nodes.

$b = 36$ is sufficient to correctly predict the mechanical response. Other variables, such as torsion, can be studied in more detail

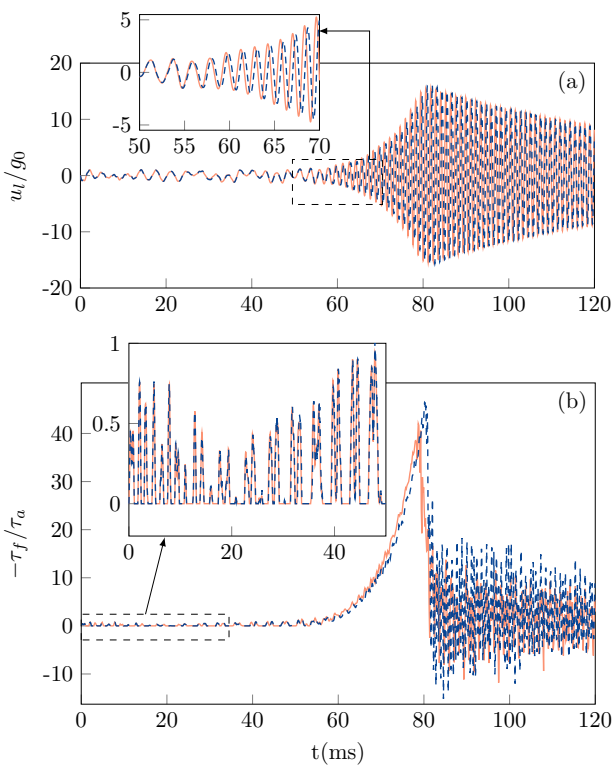

FIGURE 7: Convergence analysis on (a) labyrinth displacement and (b) frictional torque for $b = 36$ (——) and $b = 72$ (– –).

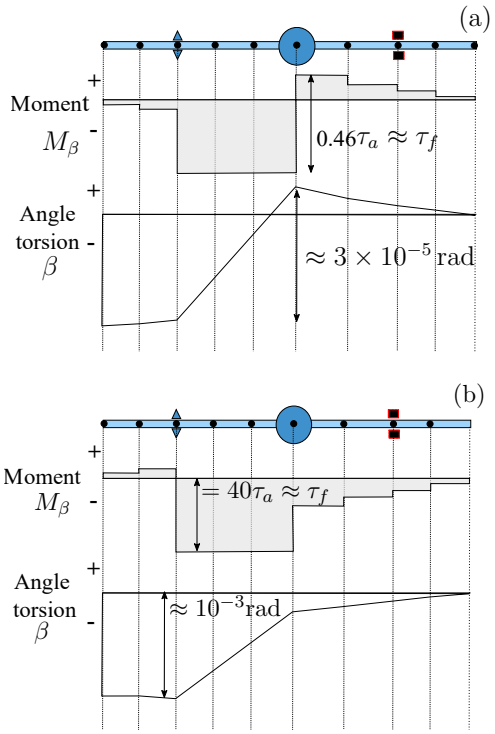

FIGURE 8: Torsion rotations and moment diagrams along the shaft line for (a) partial contact phase and (b) end of dry whip (not scaled)

with the coarser model ($b = 36$). The torsional displacement can be obtained by differentiating the rotation on element e: $\Delta\beta^e = \theta_w^{e+1} - \theta_w^e$, $e = 1, \ldots, 9$. The torsion moment by element then writes $M_\beta^e = GI_p\Delta\beta^e/\ell_e$, where ℓ_e stands for the element length.

The torsion transients for the three elements located between the labyrinth and the disk follow the same time profile as the friction torque. During the partial contact phase, these angles undergo successive cancellations and are very small during contacts. The cumulative torsion angle on these three elements is about 3×10^{-5} rad as described in Figure 8(a). This value then increases to reach 10^{-3} rad for the dry whip see Figure 8(b). Although these torsion angles are very small, the diagram of moments in Figure 8(a) indicates that the torsion moment M_β for the shaft in Inconel has maximum value of $0.04\tau_a$ downstream of the turbine disk and $-0.46\tau_a$ between the labyrinth and the disk. The resulting torsion moment applied on the disc has the same order of magnitude than the frictional torque $\tau_f (\approx -0.5\tau_a)$, see zoom in Figure 7, during the partial contact phase. At the end of dry whip, the torsion moment is about $40\tau_a$ and is resistive (i.e. < 0) everywhere downstream of the labyrinth, just like τ_f . It should also be noted that torsion moments are very low at the shaft ends, consistent with the free-free configuration of the structure. In terms of stress, the shear caused by torsion is calculated as $\sigma = M_\beta r_e/I_p$, where r_e and I_p represent respectively the outer radius and the polar area moment of the hollow circular section of the shaft. The stress is then estimated around (3 MPa) in partial contact and is 100 times higher at the end of dry whip. Although this seems high, the yield strength for Inconel can exceed (1000 MPa) if heat-treated. Therefore, although the rotorshaft geometry remains simplified by flexible beams with constant section, the predicted solution indicates the great torsional rigidity of the shaft. It is conceivable that torsion can be eliminated without disturbing the transient rotational speed.

5.2 Full Spectrogram

A frequency analysis is performed for this industrial application to characterize the triggering of dry whip. Previous work by the authors indicated that the main lines of the spectrogram of the labyrinth vibration corresponded to coupled modes of the rigid turbine and stator [13]. Defining the rotor-stator coupling in the complete system modeled with finite elements is more delicate. Initially, the rotor and stator are connected here by a common node. Indeed, node l on the shaft line corresponding to the labyrinth is merged with the master node i of the housing arbitrarily chosen at $\phi = 270°$. This connection then leads to the constraints definition $u_l = u_i$ and $v_l = v_i$ into the equations of motion. The Campbell diagram in the fixed frame is filtered to highlight modes dependent to Ω. The direct modes are noted (FW1, FW2, FW3, FW4, and FW5) and reverse modes (BW1) in Figure 9. Most of the modes are not double at zero rotational speed because the simplified coupling breaks the symmetry of the structure. Thus, some modes are likely missing. Despite its simplicity, this coupling model provides initial results. As illustrated in Figure 10, there is already an overlap between the temporal evolution of the modes and the complete spectrogram of the labyrinth vibration in the inertial frame (u_l, v_l). Notably, one of

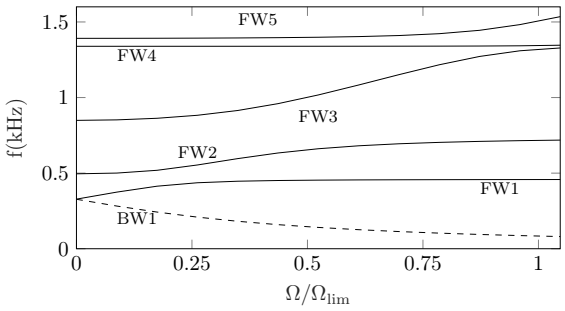

FIGURE 9: Filtered Campbell diagram of coupled rotor-stator system by node pairing, illustrating backward mode (- -): BW1 and forward modes (——): FW1, FW2, FW3, FW4 et FW5

the main lines in the negative frequency domain corresponds to the first reverse precession mode BW1. Despite introducing structural flexibility, the rigid body modes are the most solicited during rotor-stator contact. This result is expected since the turbine is more massive than the housing ring and therefore less prone to bending. However, the Figure 10 shows a second peak in the backward domain below BW1. It shifts from −420 Hz to −800 Hz with intensity increasing over time but it is not associated with any mode from Figure 9. It turns out that this unidentified mode have more complex topology that cannot be captured by a single node coupling approach. Additionally, there are overlaps with direct modes FW3 and FW5, but these lines are secondary, and their amplitude diminishes over time. This spectrogram confirms

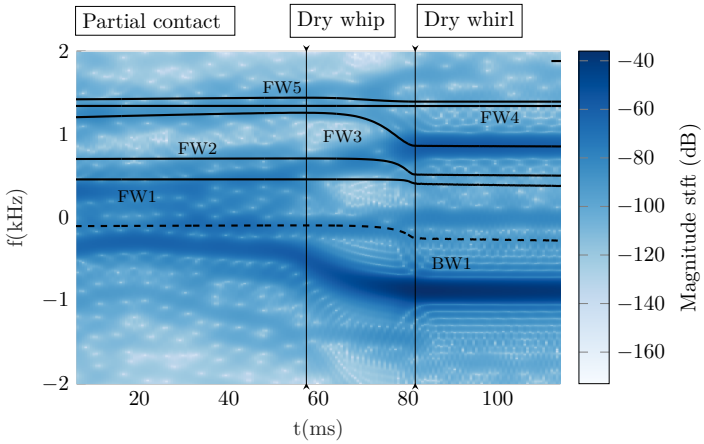

FIGURE 10: Spectrogram of labyrinth node vibration along with inverse modes (- -): BW1 and direct modes (——): FW1, FW2, FW3, FW4 et FW5

that dynamics of the rotor-stator system consist of a succession of vibrational regimes:

1. Partial contact, initially in the direct direction but quickly switching to the reverse direction;
2. Then permanent contact in dry whip;
3. Finally, a transition to dry whirl is established.

5.3 Thermal solution

The total friction energy remains the same for both superelements up to $t = 80$ ms (see Figure 11). This moment marks the

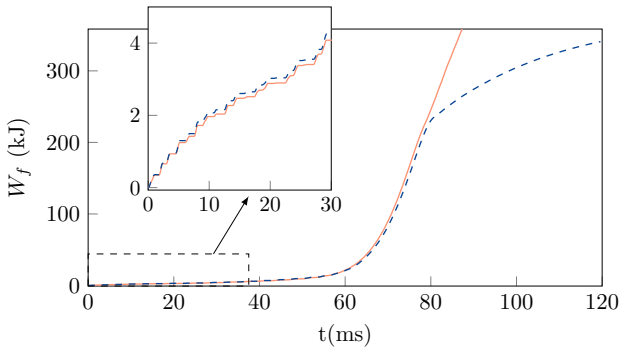

FIGURE 11: Global friction energy for $b = 36$ (——) and $b = 72$ (- -)

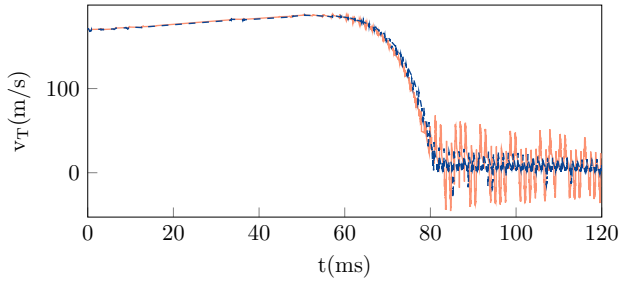

FIGURE 12: Local tangential speed at nodes with polar coordinate $\phi = 120°$ for mesh with $b = 36$ (——) and $b = 72$ (- -)

transition from an unstable dry whip regime to a stable dry whirl, as indicated by the relative speed shown in Figure 12, which trends toward zero. The inflection point in friction energy W_f is still evident. For $b = 72$, the total friction energy asymptotically approaches 360 kJ, which is half the frictional work produced with $b = 36$ by the end of the simulation. This difference arises from oscillations in relative tangential speed around zero (see Figure 12 for $b = 72$) with amplitude reduced by a factor of 2 in the finer mesh.

Temperature profiles on the contact circle are presented for three moments: 10 ms, 30 ms and 50 ms in Figure 13. With steel chosen as the material for the ring, the melting temperature T_{fus} averages 1400 °C and is indicated in the three profiles. It turns out that as early as 10 ms, the temperature exceeds the melting point in two zones at the top of the ring($\phi \approx 90°$) and at the bottom ($\phi \approx 270°$). Even though these temperatures are very high (> 4000 °C), they decrease very rapidly. At $t = 30$ ms, a few nodal temperatures have fallen below 2000 °C but conduction is too slow to justify this drop in 20 ms. The system undergoes intense heating. The slipping speed is around 170 m/s, the contact forces F_N are on the order of 1000 N, and the friction coefficient $\mu = 0.1$. Knowing that the friction power is evenly distributed between the rotor and the stator, the heat source at the nodes reaches several tens of kilowatts.

On the other hand, this heating is extremely rapid since the contact phases last less than 1 ms. The structure thus experiences very quick temperature rises and falls (see Figure 14), characteristic of so-called *flash* [37], making the temperature results quite qualitative. It is difficult to determine at this early stage of the simulation if melting actually occurs in reality. However,

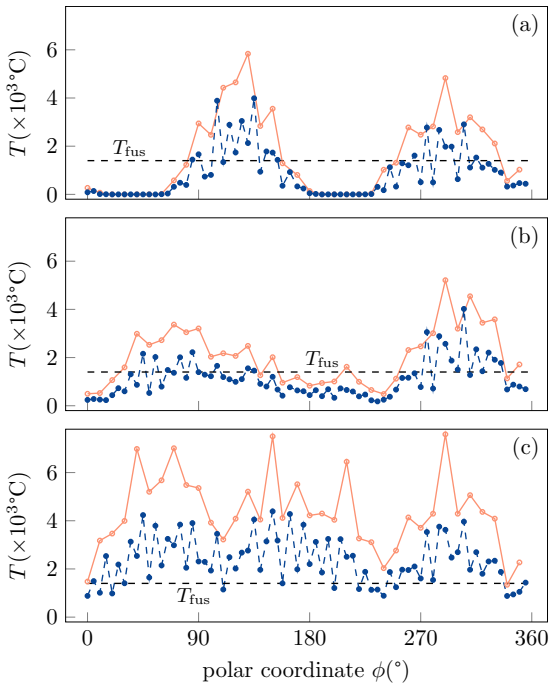

FIGURE 13: Temperature distribution at (a) $t = 10\,\text{ms}$, (b) $t = 30\,\text{ms}$ and (c) $t = 50\,\text{ms}$ with $b = 36$ (—○—) and $b = 72$ (—●—)

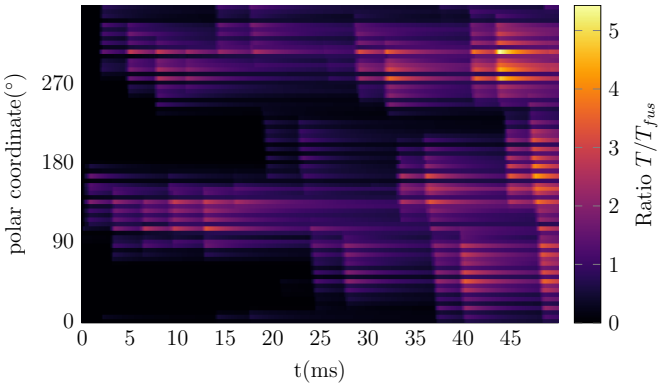

FIGURE 14: Diagram of temperature ratio (T/T_{fus}) over position and time until $t = 50ms$ for $b = 72$

over time and with each contact, the temperature inevitably increases and eventually exceeds the melting point across the entire circumference of the contact circle for $t \geq 50\,\text{ms}$.

This is why thermal expansion is never considered in the model. Such high temperatures combined with a model where displacement by expansion is linearly dependent on temperature is unrealistic and skews results. The predicted melting point is exceeded by both models, although the temperature seems generally overestimated for the coarser mesh. This may seem paradoxical given that both models provide the same global friction energy and identical resistive torque τ_f for $t \leq 80\,\text{ms}$. The normal forces are reported for three nodes positioned at $\phi = 80°$, $90°$, $100°$ on the contact circle for $b = 36$ and $b = 72$ respectively in Figures 15 and 16. For $t \leq 30\,\text{ms}$, the amplitude of the normal force at the three nodes averages 4 kN for $b = 36$, while with 72 nodes, F_N barely exceeds 2 kN. Both models predict the onset of dry whip at the same moment but again, the contact forces are lower for the refined mesh: they are capped at 100 kN versus 280 kN predicted with $b = 36$. Please note that these nodal forces represent integral quantities computed on the element surface S, which is also decreased by half with the superelement refinement. This means that, although the nodal forces decrease, the dynamical response is converged since the contact pressure F_N/S is the same for both superelements. The mechanical response is not altered, but since the nodal force locally drives the source terms of the heat equation, the thermal solution is affected. Heat and rotordynamics operate on different time and length scales. The refined mesh provides a better estimate of the temperature.

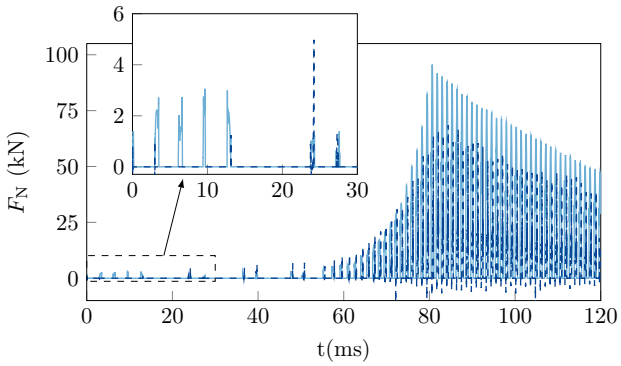

FIGURE 15: Nodal contact efforts with polar coordinates $\phi = 90°$ (—), $\phi = 100°$ (– –) for $b = 72$

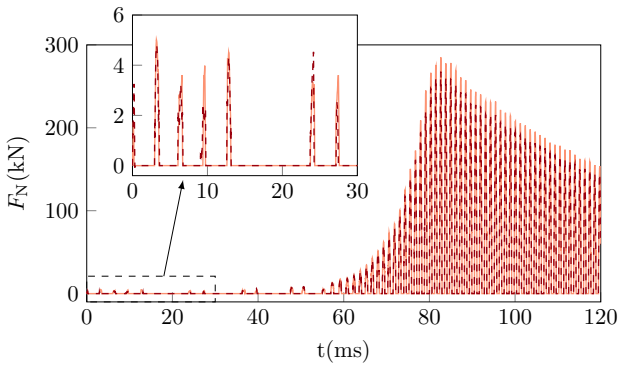

FIGURE 16: Nodal contact efforts with polar coordinates $\phi = 90°$ (—), $\phi = 100°$ (– –) for $b = 36$

The solution with $b = 72$ briefly presents negative contact forces at the end of dry whip, unlike the case where $b = 36$. Although these negative forces are nonphysical, since violating the Signorini condition $\lambda^j (= F_N^j) \geq 0$, they highlight some numerical limitations in the Carpenter algorithm. A higher number of constraints (b) may lead to a conditioning problem during the inversion of bigger matrices containing smaller values. However, the thermomechanical solution is not questioned. These few negative forces are negligible compared to the contribution of the other nodes and occur when the turbine deceleration is completed. If it is desired to ensure strictly positive forces, the Moreau-

Jean algorithm is appropriate as the constraint on the Lagrange multiplier λ^j is explicitly treated.

5.4 Sensitivity to torsion

This section considers the particular case without torsion since it might be possible that torsion has no significant effect on the solution. If eliminated, each node then only has 4 dofs, and only a single rigid body rotation φ needs to be introduced. In the following, the vector $\mathbf{q}_t$ groups only degrees of freedom in pure bending. Gyroscopic ($\mathbf{G}$) and Coriolis ($\mathbf{A}$) matrices are simplified since they are obtained by concatenations of matrices $\mathbf{A}_1^e$ and $\mathbf{G}_1^e$ respectively, and multiplied by the rigid macroscopic rotation speed $\dot{\varphi} = \Omega$ and acceleration $\ddot{\varphi}$. Additionally, resolving contact with torsion is time-consuming. For now, with 10 nodes on the shaft line and 4 dofs/node and $b = 36$ for the casing, computing 120 ms already takes over 1 hour 40 minutes without thermal effects. In this section, we propose to remove torsion and keep only the rigid body rotation φ. This simplification reduces the size of the rotor model by 20% and could notably speed up the computation of the nonlinear solution. The aim is to obtain a similar solution, particularly the transient macroscopic rotational speed from Figure 6, while achieving a computation time gain. Figure 17(a) confirms that this objective is fulfilled.

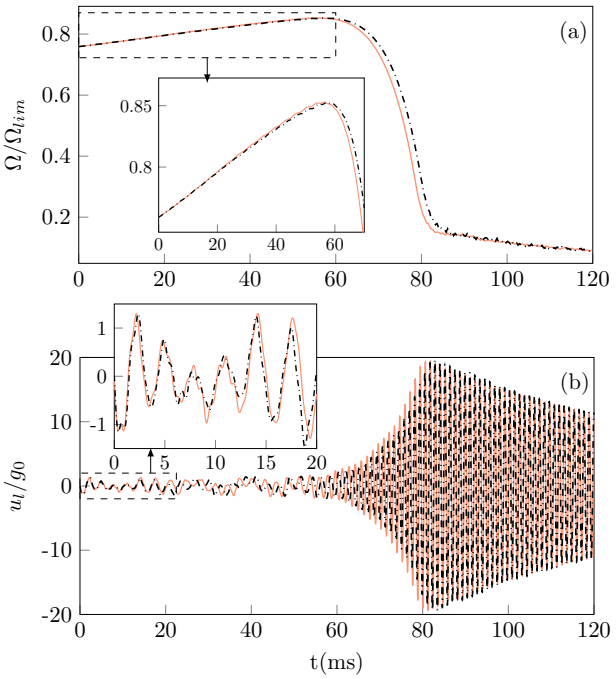

FIGURE 17: Rotational velocity (a) and labyrinth displacement (b) transients with torsion (——) and without (- - -)

Dry whip is triggered less than 2 ms later in the case without torsion, but the maximum rotational speed $\Omega_{\text{lim}} = 0.852\Omega_{\text{lim}}$ remains unchanged. During the first third of the partial contact phase (until 15 ms in Figure 18), the torque level is identical, then it becomes higher for the case without torsion. This explains why the speed profile without torsion is slightly lower just before the onset of dry whip.

Finally, the rotor vibration at the labyrinth is also compared based on the consideration or not of torsion, see Figure 17(b).

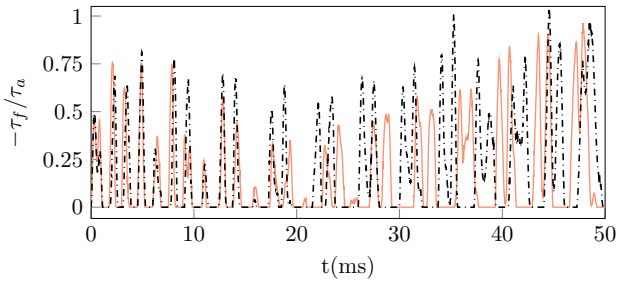

FIGURE 18: Frictional torque transient until 50 ms: with (——) and without (- - -) torsion

Again, the two responses are similar, overlapping for a shorter duration of 6 ms. They then diverge but maintain the same amplitude level. Thus, eliminating torsion from the model does not change the simulation outcome and maintains a satisfactory solution correspondence while reducing the computation time to 39 minutes, i.e., a division by 2.5.

6. CONCLUSION

Evaluating the turbine speed transient is a complex and multiphysical topic. If several works demonstrated that axial rub and/or aerodynamic effects could prevent turbine acceleration in case of loss of load, few research have been conducted yet on the management of radial rubbing contact in component mounted on the shaftline, including labyrinth seals. Given the literature of radial rotordynamics, it turns out that large contact forces can be expected in this zone.

The numerical model included a reduced and thermomechanical stator model representative of the real assembly in the engine and a standalone flexible rotorshaft accouting for flexion-torsion coupling. The transient response provided for this simplified application started in backward precessionnal motion under partial contact before turning into a dry whip regime. After the rotationnal speed drop, sliding speed remained close to zero, meaning that dry whirl regime was taking place. The mechanical results have already converged for 36 nodes, which is enough to predict speed, displacements and torque transients and spectrograms. Computation time savings are possible. Nevertheless, the thermomechanical reduction to 72 master nodes provided local quantities (relative speed at dry whirl, heat source distribution) with more precision, which is clearly reflected in the thermal solution. The high magnitude and frequency of heating cause a rapid temperature rise, followed by exponential decay in the absence of contact. The accumulation of contacts occurrences leads to temperature increase above the melting point asymptotically. The Carpenter algorithm provides verified numerical results with mesh refinement but could still present some non-physical sticking, that were mitigated in the global solution. This problem can be solved by using other solution methods, like Moreau-Jean. The case study on the rotor model showed that torsional motion does not affect the speed transient and could be eliminated from the problem, reducing calculation time.

Although the results are numerically verified, physical limitations remain due to simplifications. The significant vibration of the structures questions the structural elasticity law used in

the model. Secondary contact zones not previously considered may emerge. Furthermore, all material properties (conductivity, Young's modulus but also friction coefficient) were fixed, which is questionable given the temperature range covered during the simulation.

The proposed methodology enhances the understanding of gas turbine engines dynamics in severe operating conditions such as mechanical decoupling between compressor and turbine stages. It offers guidance for reduced-order models generation embedding complex multiphysics.

ACKNOWLEDGMENTS

The authors are grateful to Safran Helicopter Engines for providing the financial support for this project, and for giving permission to publish this work.

REFERENCES

[1] Soria, C. "Gas Turbine Shaft Over-speed/Failure Modelling. Aero/Thermodynamics Modelling and Overall Engine System Response." Ph.D. Thesis, Cranfield University. 2014. URL http://dspace.lib.cranfield.ac.uk/handle/1826/12131.

[2] Gallar, L. "Gas turbine shaft over-speed/failure performance modelling. Aero/Thermo-dynamics modelling and overall engine system response." Ph.D. Thesis, Cranfield University. 2010. URL http://dspace.lib.cranfield.ac.uk/handle/1826/8353.

[3] Psarra, A. "Gas Turbine shaft failure Modelling: friction and wear modelling of turbines in contact." Ph.D. Thesis, Cranfield University. 2010. URL http://dspace.lib.cranfield.ac.uk/handle/1826/8348.

[4] Gonzalez, A. and Pachidis, V. "On the numerical simulation of turbine blade tangling after a shaft failure." *Volume 7B: Structures and Dynamics*. 2014. ASME. DOI 10.1115/GT2014-27061.

[5] Jacquet-Richardet, G., Torkhani, M., Cartraud, P., Thouverez, F., Nouri Baranger, T., Herran, M., Gibert, C., Baguet, S., Almeida, P. and Peletan, L. "Rotor to stator contacts in turbomachines. Review and application." *Mechanical Systems and Signal Processing* Vol. 40 No. 2 (2013): pp. 401–420. DOI 10.1016/j.ymssp.2013.05.010.

[6] Muszyńska, A. *Rotordynamics*. Mechanical engineering ; 188, Taylor & Francis (2005).

[7] Choi, Y.S. "Investigation on the Whirling Motion of Full Annular Rotor Rub." *Journal of Sound and Vibration* Vol. 258 No. 1 (2002): pp. 191–198. DOI 10.1006/jsvi.2002.5091.

[8] Taher, G.A.F., Rabeih, E.A. and El-Mongy, H.H. "Experimental and numerical study of lateral vibration of rotor-stator rubbing system." *International Journal of Dynamics and Control* Vol. 12 (2024): pp. 3139–3154. DOI 10.1007/s40435-024-01425-4.

[9] Li, Z., Yao, J., Ma, L., Yang, G., Lyu, M., Wang, Y. and Wang, Z. "Analysis of the dry whirl and dry whip response in a vertical active magnetic bearing drop test rig." *Journal of Sound and Vibration* (2023)DOI https://doi.org/10.1016/j.jsv.2023.117579.

[10] Briend, Y., Chatelet, E., Dufour, R., Andrianoely, M.-A., Legrand, F., Samora Sousa, M., Steffen, V. and Baudin, S. "Dry-whip phenomenon in on-board rotordynamics: Modeling and experimentation." *Journal of Sound and Vibration* Vol. 513 (2021): p. 116398. DOI https://doi.org/10.1016/j.jsv.2021.116398.

[11] Ahmad, S. "Rotor Casing Contact Phenomenon in Rotor Dynamics — Literature Survey." *Journal of Vibration and Control* Vol. 16 No. 9 (2010): pp. 1369–1377. DOI 10.1177/1077546309341605.

[12] Jiang, J. "Determination of the global responses characteristics of a piecewise smooth dynamical system with contact." *Nonlinear Dynamics* Vol. 57 No. 3 (2009): pp. 351–361. DOI 10.1007/s11071-008-9446-z.

[13] Jacobs, C., Legrand, M., Thouverez, F. and Almeida, P. "Turbomachinery transient dynamics of radial rotor-stator contact occurrences with friction." *ASME Turbo Expo Turbomachinery Technical Conference and Exposition*: pp. 1–12. 2023. DOI 10.1115/GT2023-102198.

[14] C., Jacobs, F., Thouverez, M., Legrand and P., Almeida. "Thermomechanical Model of radial rotor-stator contact." *Journal of Sound and Vibration* Vol. 617 (2025): p. 119207. DOI https://doi.org/10.1016/j.jsv.2025.119207.

[15] Thorin, A., Guérin, N., Legrand, M., Thouverez, F. and Almeida, P. "Nonsmooth Thermoelastic Simulations of Blade–Casing Contact Interactions." *Journal of Engineering for Gas Turbines and Power* Vol. 141 No. 2 (2018): pp. 022502–1–7. DOI 10.1115/1.4040857.

[16] Chen, S.L. and Géradin, M. "Finite element simulation of nonlinear transient response due to rotor-stator contact." *Engineering Computations* Vol. 14 No. 6 (1997): pp. 591–603. DOI 10.1108/02644409710180356.

[17] Roques, S., Legrand, M., Cartraud, P., Stoisser, C. and Pierre, C. "Modeling of a rotor speed transient response with radial rubbing." *Journal of Sound and Vibration* Vol. 329 No. 5 (2010): pp. 527–546. DOI 10.1016/j.jsv.2009.09.016.

[18] Ma, H., Zhao, Q., Zhao, X., Han, Q. and Wen, B. "Dynamic characteristics analysis of a rotor–stator system under different rubbing forms." *Applied Mathematical Modelling* Vol. 39 No. 8 (2015): pp. 2392–2408. DOI 10.1016/j.apm.2014.11.009.

[19] Draganis, A. "Finite Element Modeling of Transient Thermomechanical Rolling Contact Featuring Mixed Control of the Rigid Body Motion." *Journal of Tribology* Vol. 139 No. 1 (2017): p. 011503. DOI 10.1115/1.4033048.

[20] Ireman, P., Klarbring, A. and Strömberg, N. "Finite element algorithms for thermoelastic wear problems." *European Journal of Mechanics - A/Solids* Vol. 21 No. 3 (2002): pp. 423–440. DOI 10.1016/S0997-7538(02)01208-1.

[21] Craig, R. and Bampton, M. "Coupling of substructures for dynamic analyses." *AIAA Journal* Vol. 6 No. 7 (1968): pp. 1313–1319. DOI 10.2514/3.4741.

[22] Botto, D., Zucca, S. and Gola, M.M. "Reduced-Order Models for the Calculation of Thermal Transients of Heat Conduction/Convection FE Models." *Journal of Thermal Stresses* Vol. 30 No. 8 (2007): pp. 819–839. DOI 10.1080/01495730701415806.

[23] Gao, Q., Fan, Y., Wu, Y. and Li, L. "A harmonic balance-based method to predict nonlinear forced response and temperature rise of dry friction systems including frictional heat transfer." *Nonlinear Dynamics* Vol. 111 No. 15 (2023): pp. 14263–14291. DOI 10.1007/s11071-023-08607-3.

[24] Guérin, N., Thorin, A., Thouverez, F., Legrand, M. and Almeida, P. "Thermomechanical model reduction for efficient simulations of rotor-stator contact interaction." *Journal of Engineering for Gas Turbines and Power* Vol. 141 No. 2 (2018): pp. 022501–1–9. DOI 10.1115/1.4040858.

[25] Craig, R. and Hale, A. "Block-Krylov component synthesis method for structural model reduction." *Journal of Guidance, Control, and Dynamics* Vol. 11 No. 6 (1988): pp. 562–570. DOI 10.2514/3.20353.

[26] Grimme, E.J. "Krylov Projection Methods for Model Reduction." Ph.D. Thesis, University of Illinois. 1997. URL https://theses.hal.science/tel-01711328.

[27] Wall, M.E., Rechtsteiner, A. and Rocha, L.M. *Singular value decomposition and principal component analysis*. Kluwer (2003).

[28] Fléjou, J.-L. *Code_Aster documentation: Exact elements of beams (right and curved)* (2017).

[29] Torkhani, M. *Code_Aster documentation: Gyroscopic matrices of the right beams and the discs* (2014).

[30] Sghaier, E., Bourdon, A., Remond, D., Dion, J.-L. and Peyret, N. "Dynamic Behavior of Very-High Speed Rotors at Non-stationary Conditions." *10th IFToMM International Conference on Rotor Dynamics*. Vol. 63. Springer (2019): pp. 79–90. DOI 10.1007/978-3-319-99272-3_6.

[31] Wriggers, P., Laursen, T.A., Maier, G., Salençon, J., Schneider, W., Schrefler, B. and Serafini, P. (eds.). *Computational Contact Mechanics*. Vol. 498 of *CISM International Centre for Mechanical Sciences*. Springer (2007). DOI 10.1007/978-3-211-77298-0.

[32] Carpenter, N.J., Taylor, R.L. and Katona, M.G. "Lagrange constraints for transient finite element surface contact." *International Journal for Numerical Methods in Engineering* Vol. 32 No. 1 (1991): pp. 103–128. DOI 10.1002/nme.1620320107.

[33] Legrand, M., Roques, S., Pierre, C. and Peseux, B. "Aircraft engine structural rotor-stator modal interaction." *20th ASME Biennal Conference on Mechanical Vibration and Noise*, Vol. 1: pp. 2523–2532. 2005. DOI 10.1115/DETC2005-85251.

[34] Torkhani, M., May, L. and Voinis, P. "Light, medium and heavy partial rubs during speed transients of rotating machines: Numerical simulation and experimental observation." *Mechanical Systems and Signal Processing* Vol. 29 (2012): pp. 45–66. DOI 10.1016/j.ymssp.2012.01.019.

[35] Moreau, J.-J. "Some numerical methods in multibody dynamics: application to granular materials." *European Journal of Mechanics - A/Solids* Vol. 13 No. 4 - suppl (1994): pp. 93–114. URL https://hal.science/hal-01789082.

[36] Jean, M. "The non-smooth contact dynamics method." *Computer Methods in Applied Mechanics and Engineering* Vol. 177 No. 3-4 (1999): pp. 235–257. DOI 10.1016/S0045-7825(98)00383-1.

[37] Archard, J. F. "The temperature of rubbing surfaces." *Wear* Vol. 2 No. 6 (1959): pp. 438–455. DOI 10.1016/0043-1648(59)90159-0.

APPENDIX A. TIMOSHENKO BEAM FEM MATRICES WITH TORSION-FLEXION COUPLING

Let us denote ℓ_e the length of a beam element, the shear factor $\Phi = 12EI_d/(k_{xy}GS{\ell_e}^2)$ involved in shape functions. The element mass matrices in translation involved in Equation (9) are given by

$$\mathbf{M}_u^e = \frac{\rho S\ell_e}{840(1+\Phi)^2}\begin{pmatrix} M_1 & M_3\ell_e & M_5 & -M_4\ell_e \\ & M_2{\ell_e}^2 & M_4\ell_e & M_6{\ell_e}^2 \\ & \text{Sym.} & M_1 & -M_3\ell_e \\ & & & M_2{\ell_e}^2 \end{pmatrix}$$

$$\mathbf{M}_v^e = \frac{\rho S\ell_e}{840(1+\Phi)^2}\begin{pmatrix} M_1 & -M_3\ell_e & M_5 & M_4\ell_e \\ & M_2{\ell_e}^2 & -M_4\ell_e & M_6{\ell_e}^2 \\ & \text{Sym.} & M_1 & M_3\ell_e \\ & & & M_2{\ell_e}^2 \end{pmatrix}$$

with $M_1 = 312 + 588\Phi + 280\Phi^2$, $M_2 = 8 + 14\Phi + 7\Phi^2$, $M_3 = 44+77\Phi+35\Phi^2$, $M_4 = 6+63\Phi+35\Phi^2$, $M_5 = 108+252\Phi+140\Phi^2$ and $M_6 = -(6 + 14\Phi + 7\Phi^2)$. Also, the element mass matrices related to inertia read

$$\mathbf{M}_{\theta u} = \frac{\rho I_d}{30\ell_e(1+\Phi)^2}\begin{pmatrix} 36 & -P_3\ell_e & -36 & -P_3\ell_e \\ & P_1{\ell_e}^2 & P_3\ell_e & P_2{\ell_e}^2 \\ & \text{Sym.} & 36 & P_3\ell_e \\ & & & P_1{\ell_e}^2 \end{pmatrix}$$

$$\mathbf{M}_{\theta v}^e = \frac{\rho I_d}{30\ell_e(1+\Phi)^2}\begin{pmatrix} 36 & P_3\ell_e & -36 & P_3\ell_e \\ & P_1 l^2 & -P_3\ell_e & P_2{\ell_e}^2 \\ & \text{Sym.} & 36 & -P_3\ell_e \\ & & & P_1{\ell_e}^2 \end{pmatrix}$$

with $P_1 = (4l + 5\Phi + 10\Phi^2)$, $P_2 = (-1 - 5\Phi + 5\Phi^2)$ and $P_3 = 3(1 - 5\Phi)$

The gyroscopic effect matrices are given for the case of a Timoshenko beam in bending-torsion, i.e. 10 ddls per element

$$\mathbf{A}_1^e = \alpha\begin{pmatrix} 0 & 0\,0 & 0 & 0 & 0\,0 & 0 \\ 36 & 0\,0 & P_3\ell_e & 0 & -36\,0\,0 & P_3\ell_e & 0 \\ -P_3\ell_e & 0\,0 & -P_1{\ell_e}^2 & 0 & P_3\ell_e\,0\,0 & -P_2{\ell_e}^2 & 0 \\ 0 & 0\,0 & 0 & 0 & 0\,0 & 0 & 0 \\ 0 & 0\,0 & 0 & 0 & 0\,0 & 0 & 0 \\ 0 & 0\,0 & 0 & 0 & 0\,0 & 0 & 0 \\ -36 & 0\,0 & -P_3\ell_e & 0 & 36\,0\,0 & -P_3\ell_e & 0 \\ -P_3\ell_e & 0\,0 & -P_2{\ell_e}^2 & 0 & P_3\ell_e\,0\,0 & -P_1{\ell_e}^2 & 0 \\ 0 & 0\,0 & 0 & 0 & 0\,0 & 0 & 0 \\ 0 & 0\,0 & 0 & 0 & 0\,0 & 0 & 0 \end{pmatrix}$$

and

$$\mathbf{A}_2^e = \alpha\begin{pmatrix} 0 & 0\,0 & 0 & 0 & 0\,0 & 0 & 0 \\ 18 & 0\,0 & -9\Phi\ell_e & 0 & -18\,0\,0 & P_6\ell_e & 0 \\ 9\Phi\ell_e & 0\,0 & -P_4{\ell_e}^2 & 0 & -9\Phi\ell_e\,0\,0 & -P_2{\ell_e}^2/2 & 0 \\ 0 & 0\,0 & 0 & 0 & 0\,0 & 0 & 0 \\ 0 & 0\,0 & 0 & 0 & 0\,0 & 0 & 0 \\ 0 & 0\,0 & 0 & 0 & 0\,0 & 0 & 0 \\ -18 & 0\,0 & 9\Phi\ell_e & 0 & 18\,0\,0 & -P_6\ell_e & 0 \\ -P_6\ell_e & 0\,0 & -P_2{\ell_e}^2/2 & 0 & P_6\ell_e\,0\,0 & -P_5{\ell_e}^2/2{\ell_e}^2 & 0 \\ 0 & 0\,0 & 0 & 0 & 0\,0 & 0 & 0 \\ 0 & 0\,0 & 0 & 0 & 0\,0 & 0 & 0 \end{pmatrix}$$

with $P_4 = 3 + 6\Phi + 15/2\Phi^2$, $P_5 = 2 - 2\Phi + 5\Phi^2$, $P_6 = (3 - 6\Phi)$ and $\alpha = -\rho I_p/(30\ell_e(1+\Phi)^2)$. To deduce these matrices in the absence of torsion (i.e. 8 ddls/node), delete rows/columns 5 and 10.

The coupling forces is a vector of dimension 10 with zero components except on the 5$^{\text{th}}$ and 10$^{\text{th}}$ rows. Recalling the generalized coordinates vector of the beam element $\mathbf{q}_e$, these two components respectively read $\mathbf{f}_{\text{cp}}^{e,(5)} = \ddot{\mathbf{q}}^{e\top}\mathbf{A}_2^e\mathbf{q}^e + \dot{\mathbf{q}}^{e\top}\mathbf{A}_2^e\dot{\mathbf{q}}^e$ and $\mathbf{f}_{\text{cp}}^{e,(10)} = \ddot{\mathbf{q}}^{e\top}(\mathbf{A}_1 - \mathbf{A}_2)\mathbf{q}^e + \dot{\mathbf{q}}^{e\top}(\mathbf{A}_1^e - \mathbf{A}_2^e)\dot{\mathbf{q}}^e$. When torsion is ignored, there still remains a coupling between the beam flexion and the macroscopic rotation φ. In that case, the vector $\mathbf{f}_{\text{cp}}$ is zero except on the last row and is computed by the matrix product $\ddot{\mathbf{q}}^\top\mathbf{A}\mathbf{q} + \dot{\mathbf{q}}^\top\mathbf{A}\dot{\mathbf{q}}$.

APPENDIX B. GOVERNING EQUATION OF RIGID DISC

Let us consider a rigid disc of mass m_D, polar inertia J_{pD} and diametral inertia J_{dD} with 5 dofs $\mathbf{q}_D = (u, v, \theta_u, \theta_v, \theta_w)^\top$, since axial displacement w is still neglected. Please note that these dofs also belong to the 5$^{\text{th}}$ node of the flexible shaft (see Figure 4). Matrix assembly with beam elements is simplified when the mass matrix is written with constant components. Consequently, angular acceleration effects are reflected by the Coriolis matrix $\mathbf{A}_D$ and a coupling vector $\mathbf{f}_{\text{cp},D}$ such that the disc motion is described by the differential equation

$$\mathbf{M}_D\ddot{\mathbf{q}}_D + \dot{\theta}_w\mathbf{G}_D\dot{\mathbf{q}}_D + \ddot{\theta}_w\mathbf{A}_D\mathbf{q}_D + \mathbf{f}_{\text{cp},D}(\mathbf{q}_D, \dot{\mathbf{q}}_D, \ddot{\mathbf{q}}_D) = \mathbf{0} \quad (16)$$

where $\mathbf{M}_D = \text{diag}(m_D, m_D, m_D, J_{dD}, J_{dD}, J_{pD})$ and

$$\mathbf{A}_D = \begin{pmatrix} 0 & 0 & 0 & 0 & 0 & 0 \\ 0 & 0 & 0 & 0 & 0 & 0 \\ 0 & 0 & 0 & 0 & 0 & 0 \\ 0 & 0 & 0 & 0 & J_{pD} & 0 \\ 0 & 0 & 0 & 0 & 0 & 0 \\ 0 & 0 & 0 & 0 & 0 & 0 \end{pmatrix}, \mathbf{f}_{\text{cp},D} = J_{pD}\begin{pmatrix} 0 \\ 0 \\ 0 \\ 0 \\ 0 \\ \ddot{\theta}_u\theta_v + \dot{\theta}_u\dot{\theta}_v \end{pmatrix}.$$